# Stark-induced x-ray emission from H-like and He-like Rydberg ions

M. A. Gearba, R. A. Komara, and S. R. Lundeen
*Department of Physics, Colorado State University, Fort Collins, Colorado 80523, USA*

C. W. Fehrenbach and B. D. DePaola
*Department of Physics, Kansas State University, Manhattan, Kansas 66506, USA*
(Received 8 August 2004; published 31 January 2005)

The influence of small electric fields on the x-ray spectrum emitted by highly excited Rydberg ions formed in charge capture by bare and hydrogenic ions on Rydberg atoms is studied systematically. The branching ratio to direct decay to the 1*S* ground state of the H-like and He-like product ions is observed to saturate at electric fields which are on the order of 10 V/cm and which scale approximately as $(Q/n)^5$ where $Q$ is the product ion's core charge and $n$ is the principal quantum number of the emitting levels. The limiting value of this branching ratio is sensitive to the degree of population alignment, and is found to be in good agreement with models that begin with classical trajectory Monte Carlo estimates of the alignment. The data indicate that multiple collisions with the Rydberg target are a significant factor and may alter the degree of alignment after the initial capture.

DOI: 10.1103/PhysRevA.71.013424 PACS number(s): 32.60.+i, 34.70.+e, 32.30.Rj

## I. INTRODUCTION

Highly charged ions readily capture electrons from highly excited atoms, leading to highly excited Rydberg ions which can radiate substantial amounts of energy in their subsequent decay to ground levels. For example, a fully stripped silicon ion captures an electron from an $n_T=10$ neutral atom with a capture cross section of about $10^5 a_0^2$, forming hydrogenic silicon ions with $n$ around 76 [1]. Each such capture can lead to the emission of 2600 eV of energy in the form of photons. This can be an important energy transfer process in hot plasmas containing both highly charged ions and highly excited atoms. The rate of decay and the cascade decay paths of Rydberg ions formed in this way are determined by the initial population distributions. In the absence of external fields, the $L$ and $n$ distributions are most critical. However, in the presence of relatively small electric fields, full Stark mixing of the Rydberg manifolds can occur, altering both the rate of decay and the branching ratios. When this occurs, the $m$ distribution, or alignment of the population with respect to the field direction, becomes critical. Since a high degree of alignment has been predicted theoretically for such captures, the influence of Stark mixing on the emitted radiation can be pronounced. A recent study [2] has shown that fields as small as 10 V/cm can appreciably affect the x-ray spectrum emitted from H-like and He-like Rydberg ions and confirmed a high degree of alignment in the capture process. This report extends and improves the previous study, including a range of charge capture targets ($n_T=8,9,10,12,14$) and a range of highly charged ions ($Ne^{10+}$,$Si^{13+}$,$Si^{14+}$,$Ar^{17+}$). The experimental information reveals significant features of the process, some of which confirm and refine the theoretical model used to interpret the data, and some of which call for further study.

## II. APPARATUS

The experimental setup used for the Stark-induced emission studies is illustrated schematically in Fig. 1. Bare or hydrogenic ion beams of Ne, Si, and Ar are obtained from the Kansas State University CRYEBIS ion source [3]. The beam energies were 1 keV/$Q$ in all cases, giving velocities of approximately 0.14 a.u. The ion beam is collimated to 2 mm diameter before colliding with a dense Rb Rydberg target [4]. After collision, the H-like or He-like product ions pass through a short field-free region (~28 mm) and then enter a region of static electric field (~18 mm), parallel to the ion beam direction. At the midpoint of this electric field region, the beam is viewed by a solid-state x-ray detector (model Amptek 100CR), the front face of which is 13 mm from the beam axis. After the electric field region, the beam is charge analyzed by a set of deflection plates, and incident on a two-dimensional $2-D$ position-sensitive detector (PSD). The system pressure is maintained at $\approx 10^{-7}$ Torr.

The details of the field-free and electric field regions, shown in Fig. 1, illustrate some modifications made to the apparatus used for the previous studies [2]. The first modification was to enclose the field-free region with a grounded

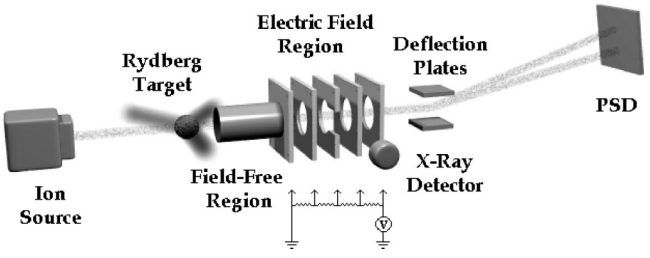


FIG. 1. Schematic representation of the apparatus. The ion beam passes through a dense Rb Rydberg target capturing an electron into a highly excited Rydberg state. After collision the beam passes through a field-free region and then it enters the detection region where it is subjected to an electric field, parallel to its propagation direction. In this region, the beam is viewed by a solid-state x-ray detector. After exiting the electric field region, the beam passes through a set of deflection plates where it is charge analyzed and then is incident on a 2D position-sensitive detector.

 

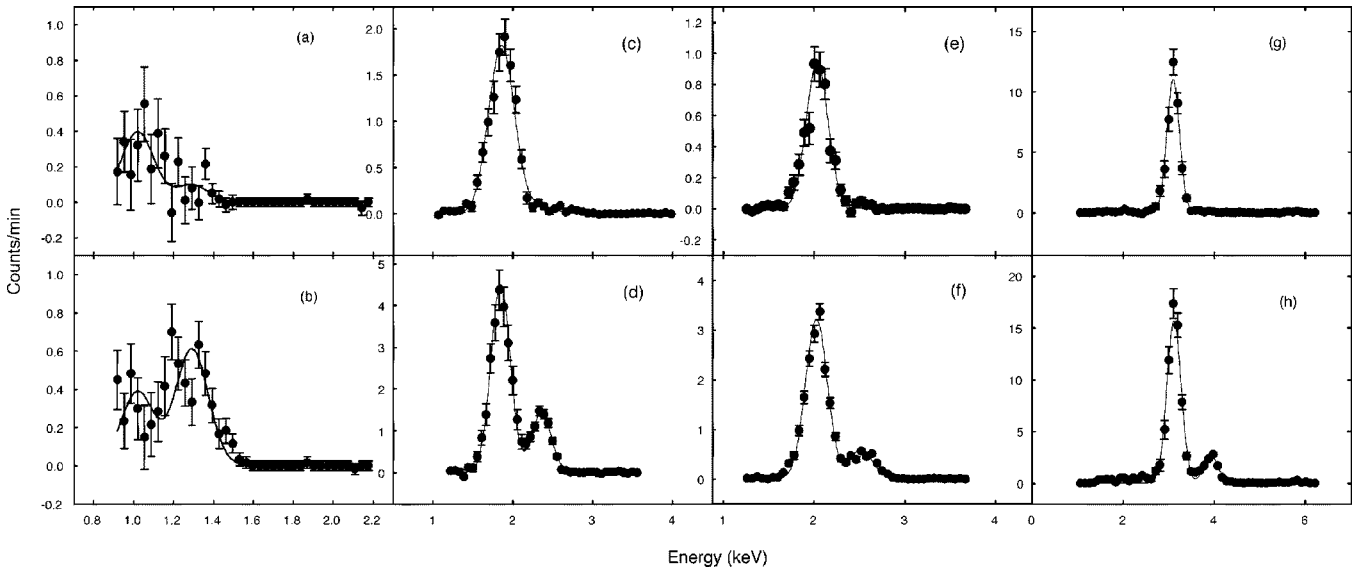


FIG. 2. Typical x-ray spectra obtained for beams of $Ne^{10+}$ (a), (b), $Si^{13+}$ (c), (d), $Si^{14+}$ (e), (f), and $Ar^{17+}$ (g), (h), incident on an $n=10$ Rb Rydberg target. (a), (c), (e), and (g) were obtained without applying any electric field in the detection region, while (b), (d), (f), and (h) were obtained for applied electric fields of 28, 21, 14, and 33 V/cm, respectively. The main peak in each spectrum represents the $K\alpha$ from $n=2$ to 1 decay. The second peak, appearing as a result of the electric field, is due to the direct decay from high Rydberg states to the ground state.

tube, 20 mm in length and 9 mm in diameter, enclosed with a $\mu$-metal shield that reduced the Earth's magnetic field by two orders of magnitude. The electric field region consists of five rectangular electrodes ($19\times35$ mm$^2$) equally spaced by 4.5 mm. The 9-mm-diameter holes in the centers of the electrodes allow passage of the ion beam, while effectively blocking the x-ray detector from direct view of the Rydberg target or of the beam downstream of the electric field region. In the original setup the field of view of the x-ray detector extended throughout the whole electric field region, which was accomplished by a horizontal gap (6 mm in height) machined in the three central electrodes [2]. In the newer geometry the field of view of the x-ray detector is reduced, by having the gap only in the central electrode. A third modification to the original apparatus consisted of adding a copper mesh of 35 lines/cm on the hole of the first electrode to ensure a rapid turn-on of the electric field. In retrospect, these revisions appear to have had little effect on the behavior under study.

The Rydberg target is formed by three-step laser excitation of a beam of thermal Rb atoms. The first excitation step is provided by a 780 nm diode laser which excites $^{85}$Rb atoms from the $5\,^2S_{1/2}$ ($F=3$) ground state to the $5\,^2P_{3/2}$ ($F=4$) excited state. The second step is provided by a 1529 nm diode laser which further excites atoms to the $4\,^2D_{5/2}$ ($F=5$) state. The last step in the excitation process is provided by a Ti:sapphire laser whose tunable wavelength allows excitation to the $n_T\,^2F_{7/2}$ ($F=6$) state, where $n_T$ ranges from 8 to 14. Approximately half the excited population is transferred to the $(n_T+1)\,^2D_{5/2}$ state by spontaneous mirrorless maser action [4]. The total excited-state thickness is estimated to be approximately $10^9$ atoms/cm$^2$. The capture fraction from the Rydberg target for these ions ranged from 1% to about 30%, depending on the choice of target, the Rb oven temperature, and the laser intensities.

This apparatus allows the x-ray and the PSD spectra to be measured simultaneously, and recorded in event mode. There was a substantial amount of background charge capture mainly from ground-state Rb in the thermal beam. In order to facilitate background subtraction, the third laser in the Rb target excitation scheme was mechanically chopped, and a gate synchronous with this reference signal allowed both x-ray and PSD spectra to be sorted with respect to the Rydberg target being on or off. Typical PSD spectra recorded both with the Rydberg target on and off as well as the difference spectrum are presented in Fig. 2 of Ref. [2]. The PSD information extracted from the difference spectrum was used to determine the charge capture fraction due to the Rydberg target. Note that the PSD information is available only when the field applied on the electrodes does not exceed 20 V/cm. For higher applied fields, the defocusing effects of the electric fields prevent resolution of the charge transfer and primary beams. The x-ray spectrum is also sorted into target-on and target-off spectra. In what follows, only the additional x rays produced when the target is on are considered.

## III. OBSERVATIONS

Typical x-ray spectra obtained for the four choices of ion incident on an $n_T=10$ Rb Rydberg target are presented in Fig. 2. In the upper row are spectra taken in the absence of an applied electric field, while in the lower row are spectra taken in the presence of a weak applied electric field. For example, Figs. 2(e) and 2(f) show spectra obtained with $Si^{14+}$ ions incident, and so represent the emission from H-like $Si^{13+}$ ions. In the case of Fig. 2(e), no electric field was applied in the viewing region, while Fig. 2(f) was obtained with an applied electric field of 14 V/cm. In the absence of the electric field, the x-ray spectrum is dominated by the peak lo-

TABLE I. Expected positions of the HX and LX x-ray features, and observed position of the HX feature.

| Primary ion | Product ion | LX assumed (keV) | HX predicted (keV) | HX observed (keV) |
|---|---|---|---|---|
| $Ne^{10+}$ | H-like Ne | 1.022 | 1.362 | 1.29(1) |
| $Si^{13+}$ | He-like Si | 1.859 | 2.437 | 2.36(1) |
| $Si^{14+}$ | H-like Si- | 2.006 | 2.673 | 2.53(1) |
| $Ar^{17+}$ | He-like Ar | 3.132 | 4.120 | 3.97(2) |

cated near 2.0 keV, which is the $K\alpha$ x ray from $n=2$ to 1 decay. The calculated value of this photon energy [5] is used to calibrate the energy scale of the detector, with higher energies determined by assuming linearity of the energy scale. The smaller peak, located near 2.6 keV, which appears when an electric field is applied, is primarily due to direct decay to the 1*S* ground state from the states populated in the charge transfer. Previous studies of the capture process [1] indicate that the charge transfer is almost resonant, so only few states near $n=76$ with binding energies of about $0.45\pm0.10$ eV are formed when $n_T=10$, as in this case. For other values of $n_T$, the populated levels change, but the change in energy is much too small to be resolved in the x-ray spectra. In fact, the resolution of the x-ray spectrum, about 300 eV, is large enough to include all members of the Lyman series down to $n=4$ in the higher-energy x-ray peak. In spite of this, we believe that this peak is primarily ($>85\%$) due to the direct decay of the high Rydberg states formed in the electron capture from the Rydberg target. For convenience, the two peaks in the x-ray spectrum will be referred to as LX (the lower-energy peak) and HX (the higher-energy peak), respectively.

The absence of the HX peak in Fig. 2(e) (no electric field in the viewing region) is expected. Recall that after collision, the ions spend about 100 ns in a field-free region before entering the field of view of the x-ray detector. Since the lifetime of the 76*P* state in the H-like Si case ($\sim$2.7 ns) is much smaller than this, the populated *P* states decay completely before entering the field of view of the x-ray detector. Once the electric field is applied, the longer-lived high-*L* states that are able to survive through the field-free region are mixed with *P* states, allowing them to decay to the 1*S* ground state and produce the HX peak. This peak evolves with the electric field, growing in strength until the field is sufficient to fully Stark mix the entire Stark manifolds of all the populated *n* manifolds. A simple estimate of the required field is obtained by setting the full width of the hydrogenic Stark manifold equal to twice the size of the *nP* fine structure splitting. This gives

$$E_S \cong \frac{\alpha^2}{6}\left(\frac{Q}{n}\right)^5 \text{a.u.} = 45\,000\left(\frac{Q}{n}\right)^5 \text{V/cm}. \qquad (1)$$

For the case of $n=76$, $Q=14$, this is about 10 V/cm. A slightly different criterion gave about a factor of 2 larger estimate in our original report [2], but with the same scaling behavior. In either case, note that these fields are much smaller than the fields that would be necessary to Stark ionize the Rydberg levels, 26 000 V/cm in this case, or even mix them with neighboring *n* levels, 1900 V/cm in this case [6].

Similar x-ray spectra are shown in Figs. 2(a)–2(d), 2(g), and 2(h) for the cases of H-like Ne, He-like Si, and He-like Ar, respectively. The x-ray spectra in Figs. 2(a), 2(c), and 2(g) were obtained without applying any field in the detection region, while the spectra in Figs. 2(b), 2(d), and 2(h) were obtained for applied electric fields of 28, 21, and 33 V/cm, respectively. The H-like Ne spectra in Figs. 2(a) and 2(b) are very poorly resolved, and also compromised by the sharp cutoff in the transmission of the detector's Be window near 1.0 keV. Nevertheless, a clear enhancement of the HX peak is seen when the electric field is applied. The observed and expected positions of the HX peaks in each spectrum are tabulated in Table I. In each case, the predicted positions are obtained using the calculated ionization energies of each ion [5] and the approximation [1]

$$E_p \cong 0.9\sqrt{Q}E_T \qquad (2)$$

where $E_T$ is the binding energy of the Rydberg target, $E_p$ is the expected average binding energy of the product ions, and $Q$ is the charge of the projectile ion. Since $E_p$ is so small, $<1$ eV, the energy of the photon emitted in direct decay to the 1*S* ground state is almost exactly equal to the ground-state binding energy. The observed positions of the HX features are slightly below the predicted positions expected if all emission originates directly from the initially populated lev-

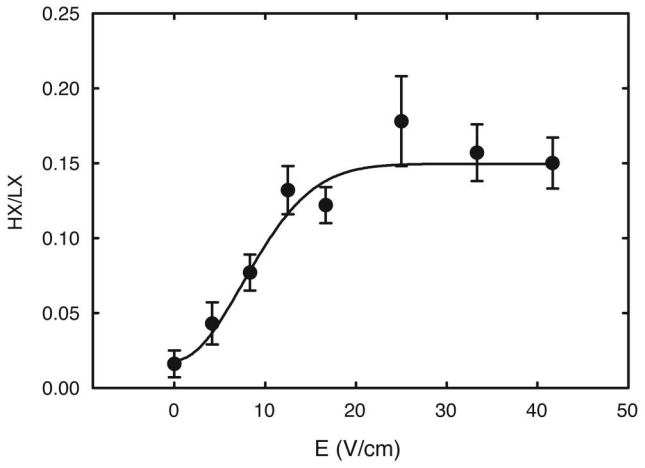


FIG. 3. The ratio between the fitted amplitudes of the HX and LX peaks as a function of the electric field for a beam of $Ar^{17+}$ incident on an $n_T=10$ Rydberg target. The smooth curve represents a fit to the experimental data described by Eq. (3).

TABLE II. Results of fits of observed values of the HX-to-LX ratio vs applied electric field to the saturation curve of Eq. (3). The data sets correspond to a 13-keV $Si^{13+}$ ion beam incident on Rydberg targets of various $n_T$. Also shown is the average charge capture fraction from the Rydberg target for each data set.

| $Q$ | $n_T$ | $R_0$ | $R_S$ | $E_S$ (V/cm) | $f_{cap}$ |
|---|---|---|---|---|---|
| 13 | 8 | 0.035(31) | 0.285(16) | 27.3(4.6) | 0.034 |
| 13 | 8 | 0.014(37) | 0.212(15) | 28.8(5.7) | 0.049 |
| 13 | 9 | 0.005(14) | 0.277(10) | 14.3(1.6) | 0.032 |
| 13 | 10* | 0.031(17) | 0.246(25) | 8.6(2.3) | 0.122 |
| 13 | 10 | 0.023(17) | 0.181(9) | 8.9(1.4) | 0.220 |
| 13 | 12 | 0.040(17) | 0.303(40) | 8.9(1.7) | 0.149 |
| 13 | 12 | 0.036(10) | 0.174(10) | 4.9(0.8) | 0.380 |
| 13 | 14 | 0.045(7) | 0.251(31) | 6.9(1.1) | 0.392 |
| 13 | 14 | 0.063(18) | 0.283(15) | 4.5(0.7) | 0.155 |
| 13 | 14 | 0.025(22) | 0.201(37) | 3.9(1.1) | 0.288 |
| 13 | 14 | 0.023(19) | 0.202(31) | 4.4(1.1) | 0.297 |

els. This is consistent with estimates of a small mixture of lower members of the Lyman series, as discussed in more detail below.

The behavior of the x-ray spectra under the influence of the electric field can be monitored by plotting the ratio between the amplitudes of the HX and LX x-ray features as a function of the electric field. For this purpose, the two peaks are fitted to Gaussians. The ratio of the fitted amplitudes for a range of applied fields is illustrated in Fig. 3 for the case of He-like Ar and an $n_T=10$ Rydberg target. The measurements in Fig. 3 have been fitted to a saturation curve of the form

$$f(E) = R_0 + (R_S - R_0)\left\{1 - \exp\left[-\left(\frac{E}{E_S}\right)^2\right]\right\}. \qquad (3)$$

The parameters of interest resulting from this fit are $E_S$, the field required to reach 67% saturation, and $R_S$, the limiting value of the HX-to-LX ratio. The parameter $R_0$ represents the HX-to-LX ratio at zero electric field, which is expected to be zero. The functional form of Eq. (3) is not supported by detailed theoretical simulation of the Stark mixing process, but was found empirically to give a good fit to the data patterns observed.

### A. $n_T$ dependence

To investigate the $n_T$ dependence, a beam of hydrogenic silicon ($Si^{13+}$) was chosen and the quantum number of the target was varied by varying the wavelength of the third laser in the excitation process. For each target, the HX-to-LX ratio was plotted versus the applied electric field. Each set of data was fitted with the saturation curve described by Eq. (3) and values for the saturation field $E_S$ and saturation ratio $R_S$ were extracted. In most cases, more than one complete saturation curve was taken for each choice of target. These raw fit results are shown in Table II. Anticipating the importance of the Rydberg target thickness, the average capture fraction from the Rydberg target, $f_{cap}$, is also shown for each data set. This increased with $n_T$, and also varied from day to day due to the condition of the Rb oven and the excitation lasers. The data set marked by an asterisk was obtained with the original detection geometry [2].

### B. $Q$ dependence

To investigate the $Q$ dependence, an $n_T=10$ target was chosen and projectile beams of $Ne^{10+}$, $Si^{13+}$, $Si^{14+}$, and $Ar^{17+}$ were used. The range in $Q$ was limited on the low side by the entrance window of the x-ray detector which cuts off photons with energies below 1.0 keV and on the high side by the CRYEBIS beam intensities. Since the total detection efficiency for x rays was about $10^{-4}$ per charge transfer event and around 5000 detected x rays were required to form an acceptable spectrum, beam intensities of around 1 pA were required to accumulate a spectrum within 30 min. For each projectile the HX-to-LX ratio was plotted as a function of the applied electric field and the data were fitted to Eq. (3) to extract values for the saturation ratio and the saturation field. Table III shows the results for $Q=10$, 14, and 17. Again the data set marked with an asterisk was obtained with the original detection geometry [2]. Results for $Q=13$ are given in Table II.

### C. Systematic corrections

Two significant systematic corrections must be applied before comparing these results with theory. The first of these is a correction for the variation of the detector efficiency with x-ray energy. This is expected to be dominated by the variation in transmission of the "0.5 mil" beryllium window covering the silicon detector. According to the manufacturer (Amptek) this consists of a 12.7-μm-thick Be window protected by a 1.3-μm Paralene ($H_{10}C_8$) coating. There is, in addition, a 1.5-mm-thick air space between the window and the front surface of the detector, and an approximately 0.2-mm-thick dead layer at the top surface of the Si detector. Using data on the x-ray transmission characteristics of these materials [7], the net transmission coefficient can be estimated as

TABLE III. Results of saturation fits for various projectile ions incident on an $n_T=10$ Rydberg target.

| $Q$ | $n_t$ | $R_0$ | $R_S$ | $E_S$ (V/cm) | $f$cap |
|---|---|---|---|---|---|
| 10 | 10 | 0.23(29) | 1.14(12) | 8.2(3.9) | $<0.10$ |
| 10 | 10 | 0.20(20) | 1.11(28) | 9.2(4.6) | 0.033 |
| 14 | 10* | 0.023(9) | 0.235(23) | 12.3(1.4) | 0.064 |
| 14 | 10 | 0.021(13) | 0.156(31) | 17.2(5.0) | 0.051 |
| 17 | 10 | 0.019(6) | 0.093(5) | 14.6(2.1) | 0.206 |
| 17 | 10 | 0.021(12) | 0.144(17) | 11.4(2.6) | 0.109 |
| 17 | 10 | 0.024(11) | 0.108(8) | 11.2(2.2) | 0.165 |

$$T=\begin{cases}(0.0812)^{[E\ (\mathrm{keV})]^{-3}} & \text{for } E<1.84\ \mathrm{keV},\\ (0.0520)^{[E\ (\mathrm{keV})]^{-3}} & \text{for } E>1.84\ \mathrm{keV},\end{cases}$$

where the discontinuity at 1.84 keV is due to the $K$ edge of Si. This transmission factor varies by about a factor of 9 over the range of x-ray energies important to this study. Clearly, this variation is sufficient to cause a noticeable change in the apparent ratio of the HX and LX x rays. The factor by which the HX-to-LX ratio is changed in this way should be different for each system studied ($Ne^{9+}$,$Si^{12+}$,$Si^{13+}$,$Ar^{16+}$), but should remain constant for all measurements with the same ion. Table IV shows the calculated values of the ratio of the transmission factor for the HX and LX x rays in each system. Since the value of the limiting value of the HX-to-LX ratio is of primary interest in this study, these factors will represent a significant correction to the raw experimental results.

A second systematic correction is more complex, but also more interesting. The value of $R_S$, the limiting ratio of HX to LX, was not entirely repeatable. Different runs, on different days sometimes found values of $R_S$ differing by nearly a factor of 2, well outside the statistical errors determined through the data fits. Further study showed that the measured value of HX to LX was strongly correlated with the thickness of the Rydberg target, which tended to vary rather widely from day to day due to the changing conditions of the Rb oven and the excitation lasers. This is illustrated in Fig. 4 which shows the decrease of HX to LX by about a factor of 2 when the fractional charge transfer produced by the Rydberg target was deliberately varied from 3% to 45%. These data were taken with a $Si^{13+}$ beam and an $n_T=10$ target at a single value of the electric field chosen to be above the saturation field.

Apparently, the capture process is not occurring under single-collision conditions at these values of target thickness, and multiple collisions with the Rydberg target are affecting the populations produced in the target. Since the value of the HX-to-LX ratio is quite sensitive to the $m$ distribution, which is expected to be far from statistical in a single-capture event, it seems likely that the subsequent collision events move the population toward a statistical $m$ distribution. A crude model for this process would consider three populations in the ion beam, $P$ the primary ion, $A$ the single-collision population, strongly peaked around $m=0$, and $B$ a fully equilibrated $m$ distribution. We could model the collisional processes transferring population between these three groups by the system of equations

$$\frac{dP}{dx}=-\rho\sigma_0 P, \tag{4a}$$

$$\frac{dA}{dx}=\rho(\sigma_0 P-\sigma_x A), \tag{4b}$$

$$\frac{dB}{dx}=\rho\sigma_x A, \tag{4c}$$

where $\sigma_0$ and $\sigma_x$ are cross sections for capture and $m$ mixing, $\rho$ is the density of the Rydberg atoms, and $x$ is the position. The solution to these equations can be approximated for small capture fractions as

TABLE IV. Calculated transmission ratios for x-ray detector window.

| System | $T$(LX) | $T$(HX) | $T$(HX)/$T$(LX) |
|---|---|---|---|
| $Ne^{9+}$ | 0.0939 | 0.369 | 3.92 |
| $Si^{12+}$ | 0.632 | 0.816 | 1.29 |
| $Si^{13+}$ | 0.691 | 0.856 | 1.24 |
| $Ar^{16+}$ | 0.891 | 0.952 | 1.07 |

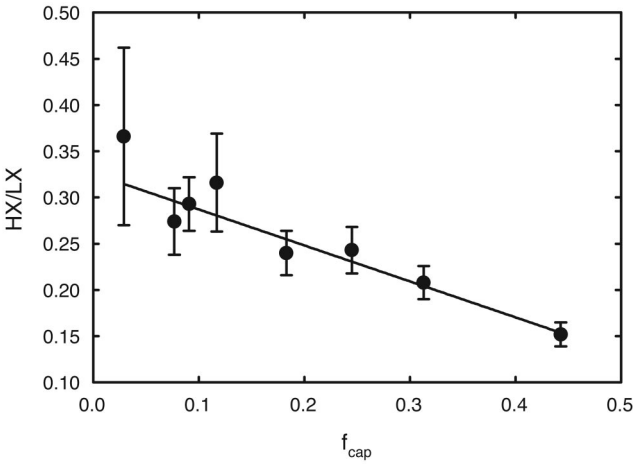


FIG. 4. Repeated measurements of the HX-to-LX ratio taken at an electric field of 19 V/cm for a beam of $Si^{13+}$ incident on an $n_T=10$ Rb Rydberg target which shows a strong correlation with the charge transfer fraction from the Rydberg target.

$$\frac{A(x)}{A(x)+B(x)} \cong 1 - \frac{1}{2}\frac{\sigma_x}{\sigma_0}[\rho\sigma_0 x]. \quad (5)$$

The quantity in square brackets represents the capture fraction $f_{\mathrm{cap}}$. If we assume, for simplicity, that the HX peak is primarily due to the $A$ population, but that both $A$ and $B$ contribute approximately equally to the LX peak, then this suggests fitting the measurements of Fig. 4 to a function of the form

$$R_S(f_{\mathrm{cap}}) = R_S^0\left(\frac{A}{A+B}\right) = R_S^0(1 - kf_{\mathrm{cap}}), \quad (6)$$

where $R_S^0$ represents the HX-to-LX ratio from the single-collision population $A$. The solid line in Fig. 4 is such a fit which gives $k=1.19(12)$, suggesting that $\sigma_x/\sigma_0=2.4$.

Whether or not this crude model is the correct explanation for the observed correlation of the measured HX-to-LX ratio with the Rydberg target thickness, some correction must be applied to the data to account for it. The data in Tables II and III also illustrate this correlation, and provide enough information to allow for such a correction. Fitting the $Q=13$, $n_T=10$, 12, and 14 data sets within Table II to Eq. (6) gave values of $k$ consistent with 1.19 in all cases. Thus, it appears that this correction factor is approximately constant with $n_T$, for a single projectile ion. We adopt the value $k=1.24(13)$, which is the weighted average of these fits and the test shown in Fig. 4. The $Q=17$ results in Table II, however, show a stronger correlation with the capture fraction, fitting to Eq. (6) with $k=2.56(33)$. This dependence on the projectile charge is pronounced, and may prove useful in confirming the physical explanation for this effect. Unfortunately, the data at $Q=10$ and $Q=14$ are not sufficient to extract independent values of this correction factor for those charges. Therefore a linear extrapolation was adopted to determine values of $k$ at $Q=10$ and $Q=14$. The results are

$$k(10) = 0.25(30),$$

$$k(13) = 1.24(13),$$

$$k(14) = 1.57(16),$$

$$k(17) = 2.56(33).$$

These correction factors were used to correct the measured $R_S$ ratios for the effects of multiple collisions. The corrected values of $R_S$ were obtained from

$$R_S^{\mathrm{corr}} = \frac{R_S}{1 - kf_{\mathrm{cap}}}\frac{T(\mathrm{LX})}{T(\mathrm{HX})} \quad (7)$$

where $R_S$ and $f_{\mathrm{cap}}$ for each saturation curve are shown in Tables II and III, the appropriate values of $k$ are shown above, and the ratio of transmissions for each ion is shown in Table IV. The weighted averages of $R_S^{\mathrm{corr}}$ and $E_S$ for each experimental configuration are summarized in Table V. Also listed in Table V are the average values of the ratio $R_0/R_S$ for each experimental configuration. These will be discussed in Sec. IV C below.

TABLE V. Average values of $R_S^{\mathrm{corr}}$, $R_0/R_S$, and $E_S$ for each experimental configuration.

| $Q$ | $n_T$ | $R_S^{\mathrm{corr}}$ | $R_0/R_S$ | $E_S$ (V/cm) |
|---|---|---|---|---|
| 13 | 8 | 0.203(28) | 0.11(9) | 27.9(3.6) |
| 13 | 9 | 0.224(8) | 0.02(5) | 14.3(1.6) |
| 13 | 10 | 0.200(14) | 0.13(6) | 8.8(1.2) |
| 13 | 12 | 0.266(23) | 0.17(4) | 5.6(1.5) |
| 13 | 14 | 0.272(17) | 0.18(3) | 4.8(0.5) |
| 10 | 10 | 0.293(28) | 0.19(15) | 8.6(3.0) |
| 14 | 10 | 0.183(36) | 0.11(4) | 12.6(1.3) |
| 17 | 10 | 0.181(13) | 0.19(4) | 12.6(1.3) |

## IV. COMPARISON WITH THEORY

In order to understand what the observations discussed above imply about the capture process, it is necessary to construct a model predicting the experimental results, starting with the population distributions expected from the initial charge capture, and including as precisely as possible the subsequent events.

### A. $R_S^{\mathrm{corr}}$, the HX-to-LX ratio at saturation

Classical trajectory Monte Carlo (CTMC) theory is probably the best theoretical description available of the initial capture process. Quantum-mechanical calculations are impractical for the high-$n$ levels populated when a highly charged ion captures an electron from a Rydberg target. In contrast, CTMC theory treats both the initial and final bound states as classical elliptical orbits and integrates the classical equations of motion through the capture event for an appropriate statistical distribution of initial states [8]. This approach has been shown to provide a practical means of obtaining expected population distributions after charge capture. Previous experimental studies have generally supported the predictions of such calculations for the $n$ distributions [1,9] and $L$ distributions [10] obtained in such captures. To illustrate, consider a 14-keV bare Si ion capturing a single electron from an $n_T=10$ Rb Rydberg target. Figure 5 shows the $n$,$L$, and $m$ distributions predicted for the capture products by CTMC simulations [11]. In this case, Eq. (2) predicts $n\sim 76$, which is a good description of the centroid of the $n$ distribution shown in Fig. 5(a). Clearly, however, a considerable range of $n$ states are predicted to be populated in the collision, and this must be taken into account in a careful description of the Stark mixing behavior. The $L$ distribution shown in Fig. 5(b) is very broad. It peaks at about $L=70$, indicating that even the highest possible $L$ levels are well populated in the collision. Far more critical to this experiment though, is the distribution of population in $m$, shown in Fig. 5(c). In contrast to the $L$ distributions of Fig. 5(b), the $m$ distribution strongly favors the lowest $m$ levels. The axis of quantization is taken along the projectile velocity. Typical $L$'s are around 60–80, but the $m$ population peaks at $m=0$ and falls to half at $m=17$. Of particular interest is the fractional population of the $|m|\leqslant 1$ levels, which in this specific

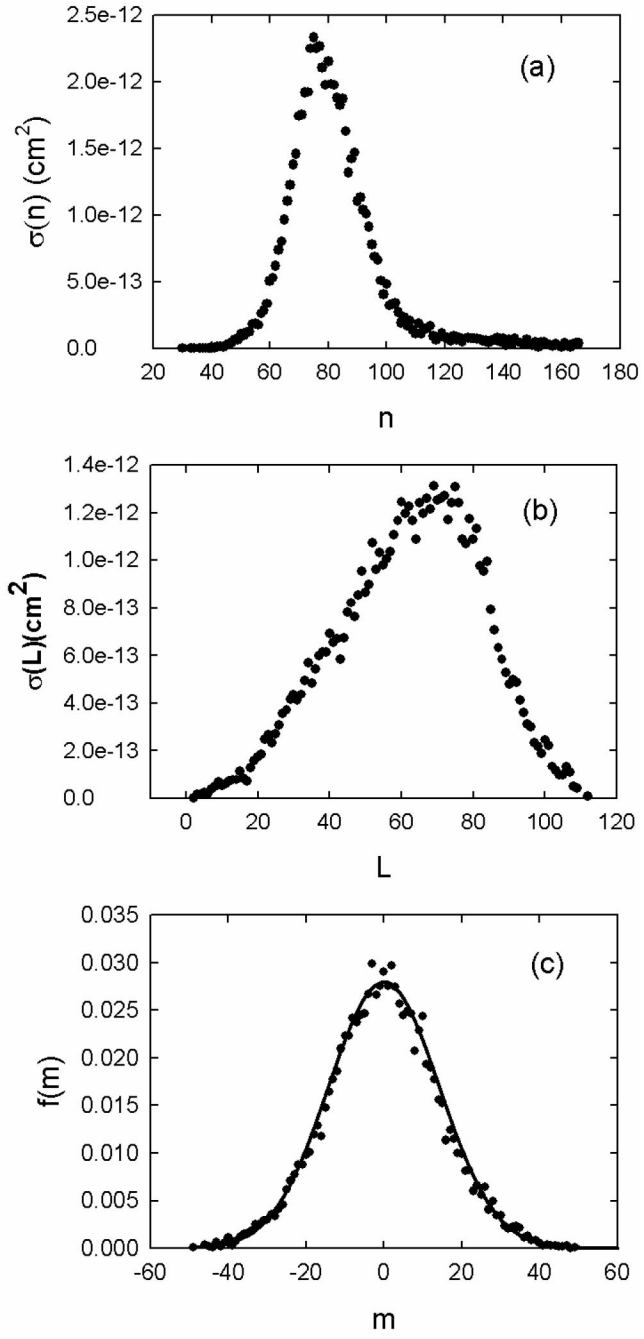


FIG. 5. Population distributions for a beam of $Si^{14+}$ incident on an $n=10$ Rb Rydberg target predicted by a standard CTMC code: (a) $n$ distribution, (b) $L$ distribution, (c) $m$ distribution. The smooth curve in (c) is a normalized Gaussian parametrization to the $m$ distribution.

case is predicted to be about 9%. The smooth curve in Fig. 5(c) is a normalized Gaussian parametrization of the $m$ distribution:

$$f(m) = ae^{-\pi a^2 m^2}. \tag{8}$$

This gives an adequate fit of the net $m$ distribution with $a=0.028$. The parameter $a$ represents the fractional population of the $m=0$ level, and $1/2a$ is the approximate value of $|m|$ where the population has fallen by a factor of 2. In what follows, it will be assumed that this parametrization applies to the population of each $n$ level separately. As a test, the $m$ distributions of the upper and lower halves of the $n$ distribution were compared, and little or no difference in those $m$ distributions was found.

In this experiment, ions that are formed in charge transfer may decay by a variety of paths. Some may decay directly to the 1$S$ ground state, others may decay by complex cascade decay paths which eventually terminate in the ground state, while still others may decay into metastable levels which do not reach the ground state before leaving the detection region. It is important to note that the x-ray detector is sensitive only to decays terminating in the 1$S$ ground state, which in hydrogenic systems are termed Lyman series decays. Decays leading to higher energy levels are below the transmission threshold of the detector window ($\sim$1 keV) and are not seen. One of the features of cascade decay paths is that they occur at an increasing rate. For example, a 76$D$ state may decay relatively slowly, but the lower $P$ or $F$ states into which it decays will decay much more rapidly. This is especially true since the initial decay will branch predominantly to the lowest possible state. This is expected to be a general feature of the cascade decay of Stark mixed Rydberg levels in weak electric fields. The initial decay will be from a Stark state, but these decays will populate states that are not Stark mixed. The subsequent cascade decays to the ground state will have much higher rates than the decay of the initial Rydberg state. Thus to model the observed Lyman series x-ray flux, the probability that an initial decay occurs within the field of view of the x-ray detector is calculated by considering the radiative decay rate and population of fully mixed Stark levels, but then all subsequent cascade decays are assumed to occur immediately. With this assumption, once the first decay occurs, it is only necessary to calculate the probability that the subsequent cascade decays result in a Lyman series x ray. So, with this view, each Rydberg decay within the detector field of view results in at most one x ray. Our model will also ignore the fact that some of the product ions are hydrogenic and others heliumlike, and treat all cases as if they were hydrogenic. In doing so, any differences in the cascade decay paths and rates of H-like and He-like ions are neglected. Also neglected are any differences in the Rydberg fine structure, an approximation that is expected to be reasonably accurate at these values of $Q$ since the relativistic contributions to the fine structure are dominant. The one clear difference between the two types of ions is that, in contrast to the H-like case, not all He-like $P$ states can decay to the $1\,^1S_0$ ground state [12]. However, since this property is shared by $P$ states of any $n$, it should not affect the ratio of HX and LX x-ray features. For simplicity, we continue to refer to the $n\rightarrow 1$ decays as "Lyman series" decays in both types of systems.

The probability of the initial decay from any particular level depends on the population of that level, the geometry of the detection region, and the level's radiative decay rate. For simplicity, the radiation will be assumed to be isotropically emitted. If $P(i)$ is the population of the $i$th level at the entrance of the electric field region, $A(i)$ is that level's radiative decay rate, and $\Omega(x)$ is the solid angle subtended by the

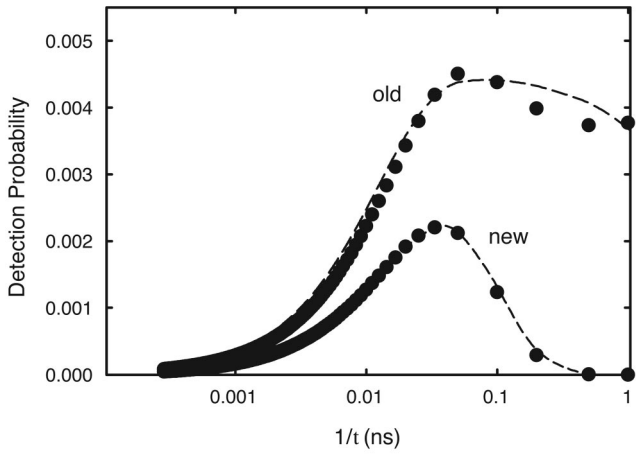


FIG. 6. X-ray detection probability vs the radiative decay rate for the two different geometries used.

x-ray detector at position $x$ within the electric field region of length $L$, then the x-ray detection probability for the $i$th level is given by

$$D(i) = \varepsilon P(i) \int_{x=0}^{x=L} A(i) \exp\left[ - A(i) \frac{x}{v} \right] \Omega(x) \frac{dx}{v}, \qquad (9)$$

where $\varepsilon$ is the detector efficiency and $v$ is the ion velocity. Since all the ions used in this study had velocities of about 0.14 a.u., the integral is simply a function of $A$, the radiative decay rate. Numerical evaluation of this integral leads to the results shown in Fig. 6. Two curves are shown, one for each of the two slightly different detection geometries used in this study. In both cases, since the total transit time through the detection region was about 60 ns, the detection probability drops toward zero when $A < 1/60$ ns. In the case of the original geometry, where the entire region was viewed by the detector, the detection probability is approximately constant for $A > 1/60$ ns. However, in the newer geometry where only the center region of the electric field region is seen by the detector, the detection efficiency drops for $A > 1/15$ ns since levels that decay this fast decay before reaching the central portion of the electric field region. In both cases, an adequate parametrization of the curves $D(A)$ was found to be

$$D(A) = D_0(1 - \exp[-AT_1])\exp[-AT_2] \qquad (10)$$

which leads to the two smooth curves shown in Fig. 6 when the parameters $(D_0, T_1, T_2)$ are taken to be

$$(D_0, T_1, T_2) = \begin{cases} (0.0045, 80 \text{ ns}, 0.2 \text{ ns}) & \text{for the old geometry,} \\ (0.0050, 34 \text{ ns}, 13 \text{ ns}) & \text{for the new geometry.} \end{cases}$$

To model the decay of the Stark mixed levels, an expression for their radiative decay rates is necessary. An approximate expression for the free radiative decay rate for hydrogenic states with $(n, L)$ with core charge $Q$ has been given by Change [13] and also by Marxer and Spruch [14]

$$A(Q,n,L) = \frac{Q^4}{n^3} \frac{(1.08 \times 10^{10} \text{ s}^{-1})}{(L + 1/2)^2} \quad (L \geqslant 1) \qquad (11)$$

and the $L = 0$ hydrogenic rate can be approximated as [15]

$$A(Q,n,L = 0) = \frac{Q^4}{n^3}(5.6 \times 10^8 \text{ s}^{-1}). \qquad (12)$$

In the presence of an electric field strong enough to completely mix all the different $L$ levels within one principal quantum number $n$, the radiative decay rates will, in general, depend on all the parabolic quantum numbers of each Stark state, $(n_1, n_2, m)$, where $n_1$ and $n_2$ are positive integers restricted by $n_1 + n_2 + |m| + 1 = n$. For example, the $n = 76$ level with $m = 0$ has $0 \leqslant n_1 \leqslant 75$. When there is a wide distribution of $L$ levels, as in this case, a wide distribution of population within these Stark levels is expected. It can be shown, using Eq. (11) and the transformation between spherical and Stark eigenstates [6], that the variation in radiative lifetime between these 76 levels is not large, typically a factor of 5. Therefore, the approximation was made that all Stark levels with a fixed value of $|m|$ decay at a single rate which is the simple average of the decay rates of all the Stark levels with that value of $|m|$. This average rate is also the average decay rate of all the field-free levels with that value of $|m|$ [6]:

$$\overline{A}(m) = \frac{1}{n - |m|} \sum_{n_1=0}^{n-|m|-1} A(n_1, m) = \frac{1}{n - |m|} \sum_{L=|m|}^{n-1} A(L, m). \qquad (13)$$

With this approximation, and using Eqs. (11) and (12), the average decay rates for each $m$ can be evaluated approximately with the results

$$\overline{A}(Q,n,m = 0) \cong \frac{Q^4}{n^4}\left[ 106 - \frac{108}{n} \right] \times 10^8 \text{ s}^{-1}, \qquad (14a)$$

$$\overline{A}(Q,n,m = 1) \cong \frac{Q^4}{(n-1)n^3}\left[ 101 - \frac{108}{n} \right] \times 10^8 \text{ s}^{-1}, \qquad (14b)$$

$$\overline{A}(Q,n,m = 2) \cong \frac{Q^4}{(n-2)n^3}\left[ 53.0 - \frac{108}{n} \right] \times 10^8 \text{ s}^{-1}, \qquad (14c)$$

$$\overline{A}(Q,n,m \geqslant 3) \cong \frac{Q^4}{n^4}\frac{108}{m} \times 10^8 \text{ s}^{-1}. \qquad (14d)$$

For the high-$n$ levels relevant to this study, these expressions are expected to be as accurate as Eqs. (11) and (12).

Using these expressions, the number of eligible "first decays" under conditions of full Stark mixing can be calculated from the calculated $n$ and $m$ distributions and the radiative decay rates characterizing each fully Stark mixed manifold:

$$N_{\text{tot}} = \sum_m N(m), \qquad (15)$$

TABLE VI. Distribution of $L$ character of decays out of fully mixed Stark manifold with $|m|=0,1,2,3$.

| $\|m\|$ level | $L=0$-like | $L=1$-like | $L=2$-like | $L=3$-like | $L>3$-like |
|---|---|---|---|---|---|
| 0 | 0.054 | 0.459 | 0.165 | 0.084 | 0.238 |
| 1 | | 0.482 | 0.173 | 0.089 | 0.256 |
| 2 | | | 0.335 | 0.171 | 0.494 |
| 3 | | | | 0.245 | 0.755 |

$$N(m) = \sum_n P(n) f(m) D(A(n,m)). \quad (16)$$

In order to predict the Lyman series spectral distribution corresponding to these decays, it is necessary to understand the "$L$ character" of these decays. For example, the decay of low-$m$ ($|m| \leqslant 1$) Stark levels is dominated by the rapid decay rate of the $P$ state. In particular, the average branching ratio of $m=0$ Stark states to "$P$-like" decay can be estimated using the equations above to be

$$b_{L=1}(n,m=0) = \frac{A_{L=1}(n,m=0)}{n\overline{A}(n,m=0)} \cong 0.453\left(1+\frac{1}{n}\right). \quad (17)$$

The result is independent of $Q$, and is approximately 0.46 for the states populated in the case illustrated in Fig. 5. In general, the average $L$ character of decays out of Stark states of a given value of $m$ can be estimated as

$$b_L(n,m) = \frac{A_L(n,m)}{(n-|m|)\overline{A}(n,m)}. \quad (18)$$

Using these expressions, the average $L$ character of decays out of Stark levels with any value of $m$ can be evaluated with the results shown in Table VI. These results are independent of $Q$ and have a weak enough $n$ dependence that they should apply to all the cases studied here.

Using the values of $N(m)$ calculated from Eq. (16) and the branching ratios from Table VI, the number of "first decays" with various $L$ characters occurring within the field of view of the detector can be calculated. In a typical case here, where the $|m| \leqslant 1$ fraction is about 9%, around 15% of these decays are $P$-like and around 67% have $L$ character of 4 or more. Note that the $L$ character of the decays, in the presence of a small electric field, depends on the $m$ distribution, not the $L$ distribution.

Once the first decay has occurred, subsequent cascades are assumed to occur immediately, and will be characterized by the same branching ratios as if the initial state had been a pure $S,P$, or $D$ state, etc. For high-$n$ states, the branching ratios to various members of the Lyman series should not depend sensitively on $n$. In our study, the LX x ray is uniquely due to the $2 \rightarrow 1$ decay, while the "HX" decay may include $n \rightarrow 1$ decays with $n \geqslant 4$. Using hydrogenic transition rates, the branching ratios from decay of each $L$ character to each of these lines and to neither of them were estimated. Here "neither" indicates either the $3 \rightarrow 1$ decay or termination of the cascade in the metastable $2S$ state. These estimates are shown in Table VII. Using these estimated branching ratios, distribution of $L$ character in the detectable first decays, the limiting value of the ratio between the HX and LX features for each experimental configuration can be estimated, with the results shown in Table VIII.

TABLE VII. Branching ratios to HX and LX of first decays with various $L$ characters.

| $L$ character | HX | LX | Neither |
|---|---|---|---|
| $L=0$ | 38% | 34% | 28% |
| $L=1$ | 79% | 6% | 15% |
| $L=2$ | 21% | 55% | 24% |
| $L=3$ | 6% | 79% | 15% |
| $L>3$ | 1% | 92% | 7% |

These predictions are compared with the experimental measurements in Fig. 7. Figure 7(a) compares the measured values of $R_S$ found in the study vs $n_T$, and shows fair agreement across the range of $n_T$ studied. In most cases, the measured ratios are about 20% larger than the model predicts. Given the approximations in the model, this is taken to be reasonable agreement. Figure 7(b) compares the values of $R_S$ found in the study vs $Q$ with $n_T=10$ and shows good agreement across the range studied. The measured ratio at $Q=10$ appears slightly high, but recall that this value is very sensitive to the correction for the transmission of the Be window on the x-ray detector so this difference could be due to a small error in the window transmission correction.

The general agreement between the measured limiting ratios of the HX and LX fluxes can be considered as confirmation of the degree of population alignment predicted by CTMC calculations to occur in the charge capture process. This is illustrated in Fig. 8 which shows the predicted ratio as a function of the $m=0$ population fraction. This figure is constructed for one specific case, $Si^{13+}$ on an $n_T=10$ target, but is typical of the other cases. For the predicted alignment, $f(0) \sim 0.03$, the $|m| \leqslant 1$ states account for about 30% of the detected x rays and the predicted HX-to-LX ratio is 0.21. If instead, the population were statistically distributed, this would correspond to a triangular $m$ distribution with $f(m=0) \sim 1/72$, and lead to an HX-to-LX ratio of about 0.14.

TABLE VIII. Predicted ratios of HX to LX at full Stark mixing.

| $Q$ | $n_T$ | Geometry | $f\ (m=0)$ | $R_S^{\text{pred}}$ |
|---|---|---|---|---|
| 13 | 8 | New | 0.0361 | 0.166 |
| 13 | 9 | New | 0.0327 | 0.194 |
| 13 | 10 | New | 0.0289 | 0.208 |
| 13 | 12 | New | 0.0234 | 0.218 |
| 13 | 14 | New | 0.0182 | 0.210 |
| 10 | 10 | New | 0.0312 | 0.223 |
| 14 | 10 | New | 0.0280 | 0.203 |
| 17 | 10 | New | 0.0277 | 0.192 |
| 13 | 10 | Old | 0.0361 | 0.200 |
| 14 | 10 | Old | 0.0280 | 0.195 |

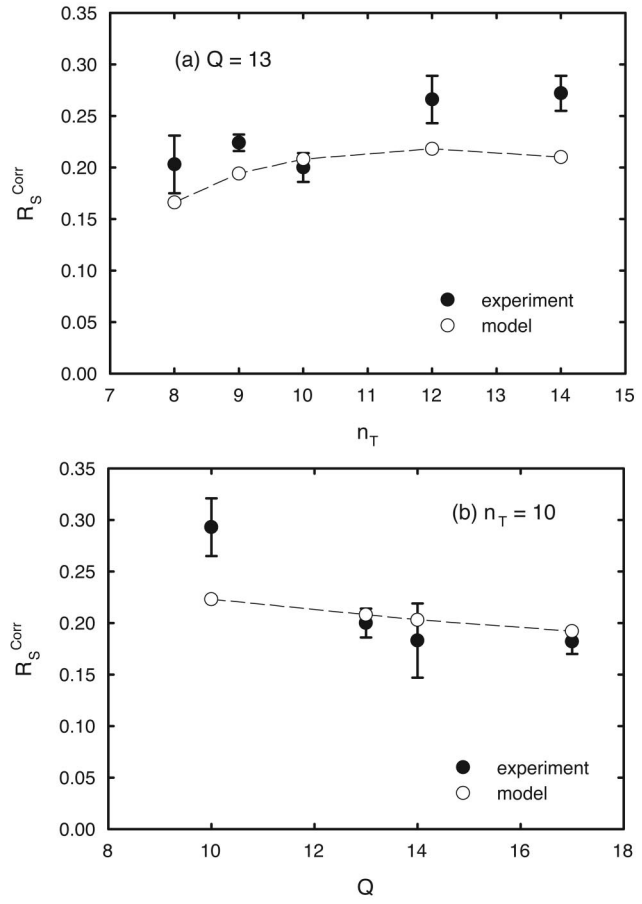


FIG. 7. HX-to-LX ratio in the saturation limit as a function of (a) quantum number of the target and (b) projectile charge. The solid points represent the experimental data corrected for transmission through the x-ray detector window and capture fraction from the Rydberg target. The open points represent the predicted values.

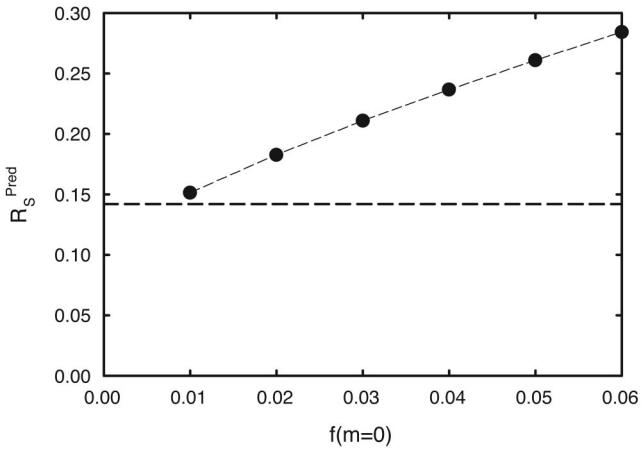


FIG. 8. HX-to-LX ratio in the saturation limit as a function of the $m=0$ population fraction shows a marked dependence on the degree of population alignment. The dotted line represents the expected saturation ratio if a statistical distribution of population were present.

The conclusion here that the "low-$m$ fraction," fractional population of $|m| \leqslant 1$ states, is about 0.09 is in contrast to the tentative conclusion reached in our earlier report [2], which suggested significantly higher low-$m$ fractions. The difference is due to a more careful modeling here of the emission process. In particular, in Ref. [2], it was assumed that only the decay of low-$m$ states could contribute to the HX peak, while here the smaller but not negligible contributions to HX from higher $m$ levels are included. This increases the expected HX-to-LX ratio, even for the same population distributions. Second, the estimate of the ratio of detection efficiencies for high-$m$ and low-$m$ states, Eq. (17) in Ref. [2], was made without the benefit of predicted population distributions. When this ratio was evaluated from CTMC $n$ and $m$ distributions, it was found to be considerably lower, more typically 0.20 instead of 0.6(2). Incorrectly assuming a high detection efficiency for high-$m$ decays led to artificially high estimates of the low-$m$ fraction from the observed x-ray ratios. Taken together, these considerations account for the contrast between conclusions in this work and the result quoted in our first study. While there is still room for improvement in the present model, current understanding is sufficient to demonstrate clearly that population alignment does occur in ion-Rydberg charge transfer, and that it is in approximate agreement with CTMC predictions.

### B. $E_S$, the saturation field

There is substantial variation in the fitted values of $E_S$ for the several configurations of the experiment, summarized in Table V. This is expected since $E_S$ should vary with the states being populated in the charge capture. A detailed description of the onset of saturation in the HX-to-LX ratio is beyond the scope of this report. It is complicated by the wide distribution of population across $n, L$, and $m$. As the electric field increases from zero, Stark manifolds of lower and lower $m$ are fully mixed, and the radiative behavior of each is altered in turn until eventually the field will mix the entire $n$ manifold. The Lyman series spectral distribution at full Stark mixing is a relatively simple aspect of this process, which is modeled by the description given above. Another relatively simple aspect is the scaling with $n$ and $Q$ of the critical mixing field for any single $n$ level. Since the width in energy of the hydrogenic Stark manifold scales like $n^2/Q$ and the hydrogenic fine structure intervals scale as $Q^4/n^3$, we would expect that the critical mixing field would scale like $(Q/n)^5$. If only a single $n$ level were populated in the charge transfer collision, such as the $n$ level implied by Eq. (2), then this scaling law could be used to check the variation of $E_S$ between the several experimental configurations. In practice, however, there is a considerable range of $n$'s populated in each capture, as Fig. 5 illustrates. Consequently, the saturation behavior is expected to be the superposition of the saturation behaviors of this range of $n$ states, and should be described by an appropriate average value of $E_S$. Since the field $E_S(n)$ is expected to scale like $n^{-5}$, the best estimate of the average $E_S$ would be

$$E_S^{\mathrm{pred}}\ (\mathrm{V/cm}) \equiv BQ^5 \frac{\sum_n N(n)\left(\frac{1}{n}\right)^5}{\sum_n N(n)}, \tag{19}$$

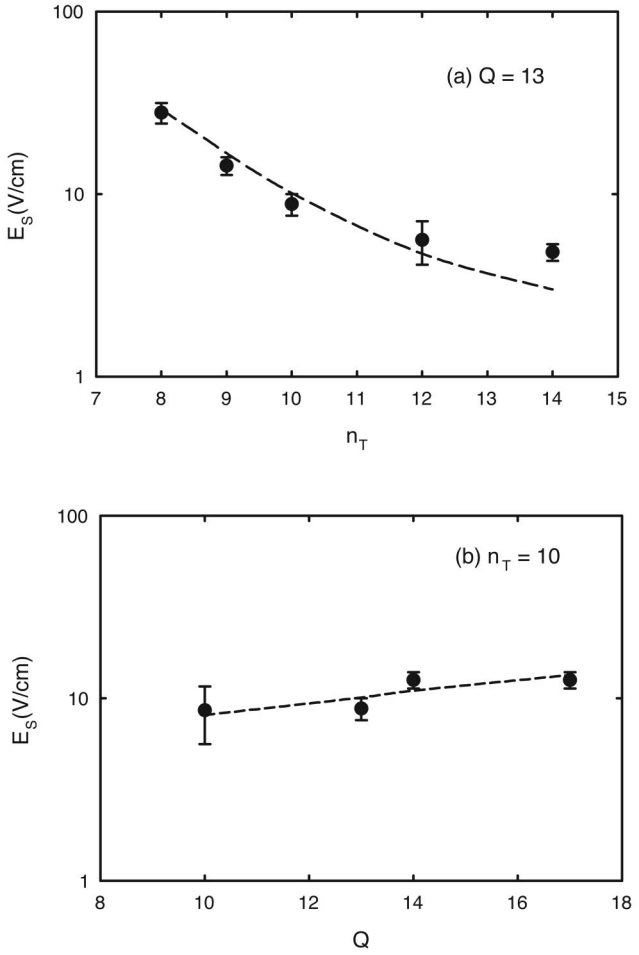


FIG. 9. Saturation field as a function of (a) quantum number of the target and (b) projectile charge. The solid points represent the experimental data. The line represents the predicted saturation field given by superposition of the $n$ states populated in the capture process.

$$N(n) = \sum_m P(n) f(m) D(A(n,m)), \tag{20}$$

where $N(n)$ measures the relative count rate from each $n$ level and $B$ is an arbitrary constant. In Eq. (1), it was estimated that $B \sim 45\,000$ V/cm, but now by comparison with observations, a more precise value can be obtained. Using the $n$ and $m$ distributions predicted by CTMC calculations, the weighting factors $N(n)$ can be computed and $E_S^{\text{pred}}$ evaluated for all of the experimental configurations up to the constant $B$. The appropriate averages over both the initial population distribution and the $n$ distribution of detected photons, $N(n)$, are summarized in the Appendix. If the constant $B$ in Eq. (19) is chosen to give the best fit to the values of $E_S$ for each configuration, the result is $B = 30\,000(2000)$V/cm, and the resulting predictions match the observations in all but one of the experimental cases. The comparison between the fields predicted by Eq. (19) with $B = 30\,000$ V/cm and the experimental results is shown in Figs. 9(a) and 9(b). The agreement is sufficient to confirm the expected scaling law.

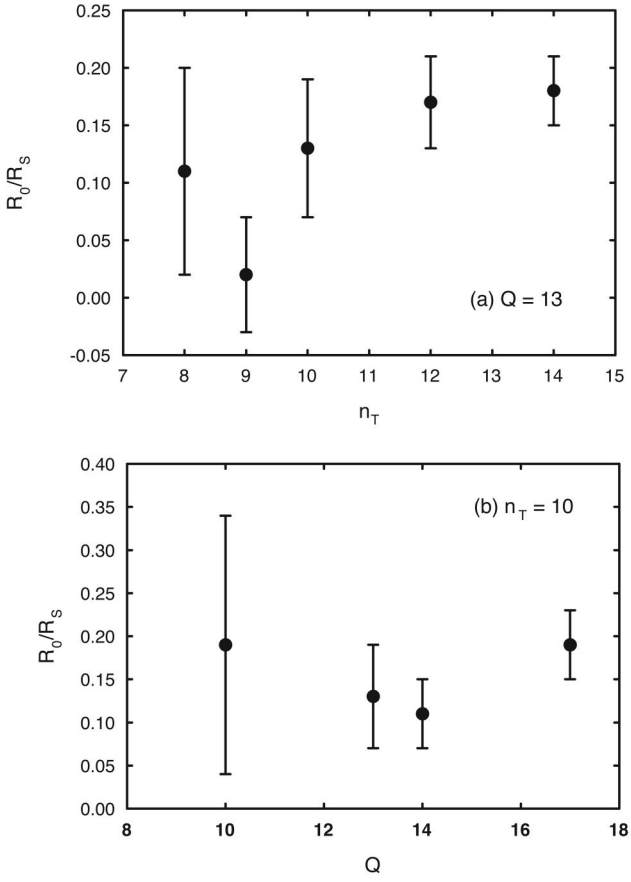


FIG. 10. Ratio between the fitted values of $R_0$ and $R_S$ as a function of (a) quantum number of the target and (b) projectile charge.

In the one discrepant case of $Q=13$, $n_T=14$, where the predicted $E_S$ is the smallest [3.0(1)V/cm], the fitted value is 4.8(5)V/cm. This is more than three standard deviations higher, but it differs by less than 2 V/cm. Anticipating the discussion of $R_0$ below, this discrepancy is comparable to the size of suspected stray electric fields, and so no great significance should be attached to it unless it can be repeated with better control of stray fields.

### C. $R_0$, HX-to-LX ratio at zero applied field

The HX-to-LX ratio with zero applied electric field is expected to be zero since the $P$ states that contribute to HX should completely decay in the 100-ns-long drift region between the Rydberg target and the electric field region. However, examination of the fitting results shown in Tables II and III show that this is not completely true. The fitted values of $R_0$ are small but in many cases not consistent with zero. A consistent value of the ratio between the fitted $R_0$ and the fitted $R_S$ is found for each experimental configuration. The weighted averages of this ratio for each configuration are shown in Table V and plotted in Fig. 10(a) for the $n_T$ study, and in Fig. 10(b) for the $Q$ study. Figure 10(a) shows that this ratio is consistent with zero for low-$n_T$ targets, but grows steadily, reaching about 0.2 for the $n_T=14$ target. Figure

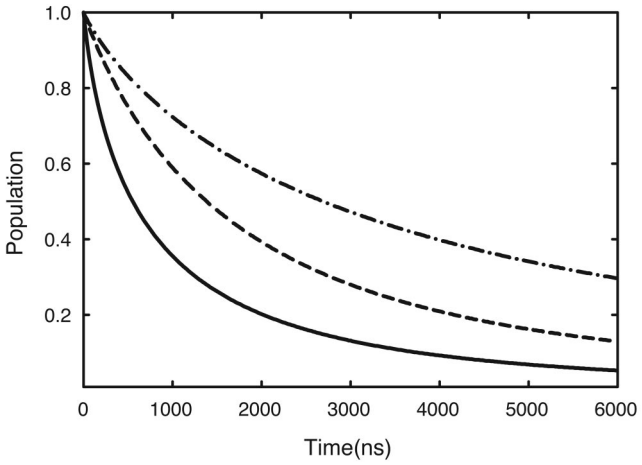


FIG. 11. Theoretical total Rydberg population vs time after capture in three different situations: dash-dotted line, free decay with the $L$ distribution from Fig. 5; dashed line, rapid collisional mixing, statistical distribution; and solid line, Stark mixing.

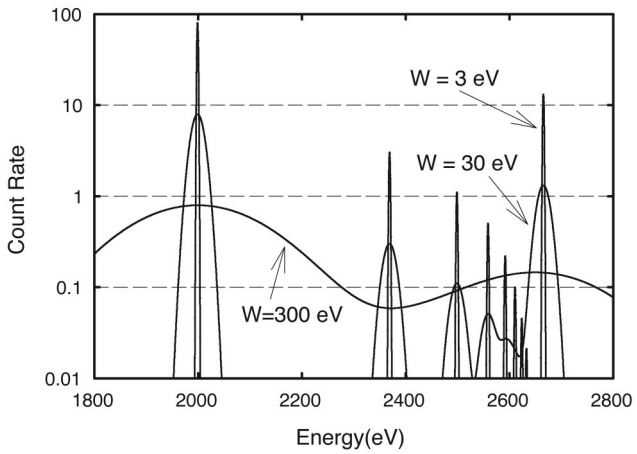


FIG. 12. Simulated x-ray spectra for different detector resolutions 300, 30, and 3 eV.

10(b) shows a ratio nearly constant with $Q$ and approximately 0.15. The reason for these nonzero values of $R_0$ is not yet fully understood.

Models starting with the population distributions predicted by CTMC calculations fully confirm the prediction that if the ions propagate in zero field, the HX strength should in fact be extremely small, essentially zero. Simulations beginning with the CTMC predictions of population distributions and including the contributions of $P, D$, and $F$ levels to the HX feature predict that, in zero field, the expected ratio is more than three orders of magnitude smaller than observed. It appears likely, therefore, that the assumption of field-free propagation is not correct.

A possible explanation for these observations is that when the applied electric field is zero, there are stray electric fields, perhaps caused by charging of the field electrodes which Stark mix the highest $n$ levels. This would account for the increase in $R_0/R_S$ as $n_T$ increases, since higher-$n_T$ targets produce higher-$n$ products which are more easily mixed. To account quantitatively for the observations, the stray fields would need to be large enough to Stark mix around 15–20% of the population produced by the $n_T=12$ and 14 targets. Examination of the $n$ distributions $N(n)$ suggests that this would require stray fields of approximately 1 V/cm if we assume that Eq. (19) with $B=30\,000$ V/cm correctly predicts the field required for any given $n$. Another factor favoring this explanation is that measurements with an $n_T=16$ target showed little change in HX-to-LX with applied field. In other words, for $Q=13$ and $n_T=16$, it was found that $R_0/R_S \geqslant 0.5$. This is also consistent with the expected effects of stray fields of about 1 V/cm. On the other hand, it should be emphasized that the HX feature is a small fraction of LX, and $R_0$ represents a small fraction of HX, so that in some cases, the apparent nonzero result for $R_0$ could be at least partly due to a failure of the LX instrumental line shape to conform to a simple Gaussian functional form. This appears to be the case for the $Q=17$ results, where the $N(n)$ distributions do not predict any substantial $R_0$.

## V. DISCUSSION

The sensitivity of x-ray emission from highly excited Rydberg atoms and ions to small electric fields is well documented by this study. The level of agreement with a relatively simple model of cascade x-ray decay from fully Stark mixed Rydberg levels is certainly sufficient to confirm the general description of the phenomenon. The close agreement with the predicted HX-to-LX ratios at full saturation (Fig. 7) demonstrates that the degree of alignment of the population along the projectile velocity axis ($\sim$9% with $|m| \leqslant 1$) is in approximate agreement with the predictions of CTMC calculations. More generally, the sensitivity of the emitted spectrum to the population alignment demonstrates that in some applications the highly nonstatistical alignment could be a significant factor in predicting or interpreting the emitted spectrum. This, in turn, focuses additional attention on processes that can tend to redistribute the $m$ populations, such as the multiple Rydberg collisions evidenced in this experiment. This experiment provides both a practical method for measuring the initial alignment and a way to study processes that alter it. Both can be valuable tools in future studies.

A general conclusion that can be drawn from this study is that both the emission rate and the branching ratios of photon emission from hydrogenic and heliumlike Rydberg atoms or ions are strong functions of the population alignment when emission takes place in the presence of electric fields comparable to those indicated by Eq. (1). In order to illustrate the effect of Stark mixing on the total emission rate, consider the population distributions represented by Fig. 5. Figure 11 illustrates the predicted time dependence of the total Rydberg population under three conditions. (1) The populations decay freely, according to the radiative lifetimes of each $n, L$ level. (2) Rapid collisional mixing maintains a statistical distribution of $L$ and $m$ states within each $n$ level throughout the decay process. (3) A weak electric field (along the collision axis) maintains Stark mixing of the populations during decay. As Fig. 11 illustrates, the total decay rate, in this case varies by almost an order of magnitude depending on conditions. Applications considering the emission rate in such an environment should consider the possible alignment. Simi-

TABLE IX. Averages derived from CTMC population distributions, and from calculated detection probabilities.

| $Q$ | $n_T$ | $1.05Q^{3/4}n_T$ | $(\langle n^{-2}\rangle_\sigma)^{1/2}$ | $(\langle n^{-2}\rangle_N)^{1/2}$ | $(\langle n^{-5}\rangle_N)^{1/5}$ |
|---|---|---|---|---|---|
| 13 | 8 | 57.5 | 56.2 | 53.9 | 52.0 |
| 13 | 9 | 64.7 | 64.7 | 60.6 | 58.0 |
| 13 | 10 | 71.9 | 73.6 | 67.5 | 64.2 |
| 13 | 12 | 86.3 | 96.2 | 80.9 | 74.7 |
| 13 | 14 | 100.6 | 117.5 | 91.0 | 81.9 |
| 10 | 10 | 59.0 | 61.2 | 54.7 | 51.6 |
| 14 | 10 | 76.0 | 78.5 | 71.7 | 68.0 |
| 17 | 10 | 87.9 | 88.5 | 82.6 | 79.3 |

larly, the branching ratios among the various possible emission wavelengths can vary substantially with alignment when Stark mixing is present.

Another interesting aspect of the present study is its potential for creating spectrally narrow, calculable x-ray sources. Although this feature is hidden in the x-ray spectra obtained with the low-resolution detector used in this study, the cascade simulations used to model the decays predict that the primary spectral feature in the HX peak is the direct decay from the initially populated states to the 1*S* ground state. The CTMC simulations of the $n$ distributions in the initial population suggest an energy width of about 0.3 eV, as illustrated for one case in Fig. 5. Of course, this presupposes a selectively excited Rydberg target whose binding energy determines the average binding energy of the product ions. If the x-ray spectrum emitted from such a population, in the presence of a weak electric field were observed with a high-resolution x-ray detector, it should reveal a very narrow feature corresponding to the direct ground-state decay of the populated levels. This is illustrated in Fig 12 which simulates emission spectra for this case, given detector resolutions of 300, 30, or 3 eV. In principle, such a narrowband x-ray source could be created at a wide range of x-ray wavelengths by the use of a slow beam of bare ions of various charges and a dense selectively excited Rydberg target. Except for a small correction due to the binding energy of the emitting Rydberg ion, the photon energy would correspond to the ground-state binding energy, which can be calculated very precisely in hydrogenic systems. Since both the width of the initial population distribution and the severity of Doppler broadening decrease with the velocity of the bare ion beam, very low-energy ion beams would be attractive in this application. Sufficiently slow beams might reach the limit where only a single principal quantum number was populated in the capture collision. If this were the case, and if the emission linewidth were limited only by the Stark width of the emitting level, the inherent linewidth could be extremely small. For example, a bare argon beam with velocity of 0.01 a.u. incident on an $n_T=8$ Rydberg target should populate $n$ states within an energy width of about 0.01 eV [1], and could therefore populate $n=74$ almost entirely. Even if several $n$ levels were populated, the fundamental emission width would be $\Delta\lambda/\lambda \sim 10^{-6}$. If only $n=74$ were populated and the emission were limited by the Stark width in the necessary electric field of 30 V/cm, the relative Stark width of the emission would be $\Delta\lambda/\lambda = 10^{-8}$. Doppler broadening would have to be carefully controlled to take full advantage of the inherent spectral width of such a source.

## ACKNOWLEDGMENTS

We thank Daniel Vrinceanu for helpful discussions, and Chris Verzani for assistance in collecting some of the data. Eric Hessels provided tabulations of hydrogenic matrix elements used for evaluating cascade branching ratios. The assistance of the staff of the J. R. Macdonald Laboratory at Kansas State University, where this work was carried out, is also gratefully acknowledged. This work was supported by the Chemical Sciences, Geosciences, and Biosciences Division of the Office of Basic Energy Sciences, Office of Science, U.S. Department of Energy.

## APPENDIX

For each experimental configuration, three averages are shown in Table IX, and compared with the result of the approximate Eq. (2) in the text which implies $n=1.05Q^{3/4}n_T$.

$(\langle n^{-2}\rangle_\sigma)^{1/2}$: averaged over the initial population distribution, this $n$ is equivalent to the average product energy.

$(\langle n^{-2}\rangle_N)^{1/2}$: averaged over the $n$ distribution of detected photons, $N(n)$, this average is biased toward the lower $n$'s which are detected more efficiently.

$(\langle n^{-5}\rangle_N)^{1/5}$: averaged over $N(n)$, this average is weighted more strongly toward lower $n$ by the higher inverse power. These averages are used to estimate the relative values of $E_S$ in the several configurations.

[1] D. S. Fisher, S. R. Lundeen, C. W. Fehrenbach, and B. D. DePaola, Phys. Rev. A **63**, 052712 (2001).
[2] M. A. Gearba, R. A. Komara, S. R. Lundeen, W. G. Sturrus, C. W. Fehrenbach, B. D. DePaola, and X. Flechard, Phys. Rev. A **66**, 032705 (2002).
[3] M. P. Stöckli *et al.*, Phys. Scr., T **71**, 188 (1997).
[4] C. W. Fehrenbach, S. R. Lundeen, and O. L. Weaver, Phys. Rev. A **51**, R910 (1995).
[5] W. C. Martin, J. R. Fuhr, D. E. Kelleher, A. Musgrove, L. Podobedova, J. Reader, E. B. Saloman, C. J. Sansonetti, W. L. Wiese, P. J. Mohr, and K. Olsen, NIST Atomic Spectra Database (version 2.0), available at http://physics.nist.gov/asd.
[6] T. F. Gallagher, *Rydberg Atoms* (Cambridge University Press, Cambridge, U.K., 1994).
[7] J. H. Hubbell and S. M. Seltzer, Tables of X-Ray Mass Attenuation Coefficients and Mass Energy-Absorption Coefficients (version 1.03), available at http://physics.nist.gov/xaamdi
[8] R. E. Olson, J. Phys. B **13**, 483 (1980).
[9] R. G. Rolfes and K. B. MacAdam, J. Phys. B **15**, 4591 (1982).
[10] S. R. Lundeen, R. A. Komara, C. W. Fehrenbach, and B. D. DePaola, Phys. Rev. A **64**, 052714 (2001).
[11] The CTMC code used here was originally written by R. E. Olson, but extensively modified by N. Toshima and later by the present authors. Calculated results were consistent with the $n, L$, and $m$ distributions reported for specific cases by J. Pascale, R. E. Olson, and C. O. Reinhold, Phys. Rev. A **42**, 5305 (1990).
[12] C. D. Lin, W. R. Johnson, and A. Dalgarno, Phys. Rev. A **15**, 154 (1977).
[13] E. S. Chang, Phys. Rev. A **31**, 495 (1985).
[14] H. Marxer and L. Spruch, Phys. Rev. A **43**, 1268 (1991).
[15] H. A. Bethe and E. Salpeter, *Quantum Mechanics of One- and Two-Electron Atoms* (Springer-Verlag, Berlin, 1957).